Nanoscale

PAPER

CrossMark
← click for updates

Tungsten oxide nanorod growth by pulsed laser deposition: influence of substrate and process conditions

Peng Huang,[†][a] M. Mazhar Ali Kalyar,[‡][a] Richard F. Webster,[b] David Cherns[b] and Michael N. R. Ashfold*[a]

Tungsten oxide nanorods (NRs) have been grown on W, Ta and Cu substrates following 193 nm pulsed laser ablation of a WO_3 target in a low background pressure of oxygen. The deposited materials were analysed by scanning and (high resolution) transmission electron microscopy (HRTEM), selected area electron diffraction (SAED), X-ray diffraction, Raman and X-ray photoemission spectroscopy, and tested for field emission. In each case, HRTEM analysis shows NR growth along the [100] direction, and clear stacking faults running along this direction (which are also revealed by streaking in the SAED pattern perpendicular to the growth axis). The NR composition in each case is thus determined as sub-stoichiometric $WO_{3-\delta}$, but the NR morphologies are very different. NRs grown on W or Ta are short (hundreds of nm in length) and have a uniform cross-section, whereas those grown on a Cu substrate are typically an order of magnitude larger, tapered, and display a branched, dendritic microstructure. Only these latter NRs give significant field emission.

1. Introduction

Tungsten oxide (WO_x, $x \leq 3$), an n-type semiconducting metal oxide with band gap $E_g \sim 2.6$–3.0 eV, attracts interest by virtue of its rich crystallography, its many attractive properties and the diversity of routes by which it can be prepared in low-dimensional nanostructured form.[1] Chromism (*i.e.* colour change in response to external stimuli such as voltage, reducing gases, heat and/or light)[2,3] is arguably its most distinctive property, with real or potential applications in smart windows, flat panel displays, optical memory and read–write–erase devices, but other reported applications of tungsten oxide films include photocatalysis,[4] water splitting,[5] gas sensing applications[6,7] and dye sensitized solar cells.[8]

WO_x structures are typically based on slightly distorted variants of the ReO_3 cubic crystal structure, with each metal atom lying at the centre of an octahedron of O atoms. Tunnels of varying shapes and sizes may thus arise. Stoichiometric WO_3 itself can exist in several different polymorphs formed by appropriate tilting and/or rotation of the constituent WO_6 octahedra without relaxing the requirement of corner sharing. As with other perovskite-based transition metal oxides, however, tungsten oxide also readily tolerates oxygen vacancies, which can coalesce to form defects (shear planes). Such WO_x ($x \leq 3$) structures necessarily consist of both edge- and corner-shared octahedra, and many stable sub-stoichiometric structures have been characterised.[1,9]

Relative to the bulk material, nanostructured WO_x samples will display an increased surface-to-volume ratio and may thus be expected to offer enhanced performance with respect to properties that are sensitive to, for example, modifications to the surface energies or possible quantum confinement effects.[1] The detailed properties of low-dimensional materials are sensitive to many factors, however, including chemical composition, thermochemical (phase) stability, crystal structure, surface morphology, porosity, *etc.*, so the exploration of different routes to forming nanostructured WO_x remains a very active area of research. Demonstrated growth methods include both solution-based (hydrothermal methods, acid-bath, sol–gel, electrodeposition, *etc.*)[1,10–14] and vapour phase approaches (*e.g.* physical vapour deposition, thermal evaporation, sputtering, *etc.*),[1,15,16] with post-annealing in oxygen or air offering further possibilities for tuning the O content, phase, and crystallinity of the as-grown material.

[a]School of Chemistry, University of Bristol, Bristol, BS8 1TS, UK.
E-mail: mike.ashfold@bris.ac.uk; Tel: +44 (0)117 9288312
[b]School of Physics, University of Bristol, Tyndall Avenue, Bristol, BS8 1TL, UK
†Permanent address: Department of Physics, Lanzhou University, Lanzhou 730000, China.
‡Permanent address: Department of Physics, University of Sargodha, Sargodha, Pakistan.

Pulsed laser deposition (PLD) has also been used to produce WO_x films,[17–23] including films composed of nanorods (NRs) on quartz substrates.[24,25] PLD offers the advantage of relatively slow growth, in a clean and dry environment. In the case of ZnO, for example, PLD constitutes a catalyst-free route to forming arrays of high quality, aligned NRs, with controllable diameter and aspect ratio.[26,27] Here, we show that PLD also offers a route to forming WO_x NRs on a range of metal substrates (tungsten, tantalum and copper), and explore the sensitivity of the deposition process to conditions like substrate temperature, O_2 pressure, and incident fluence. The present study confirms that WO_x NRs can be grown on each of these substrates with just subtle changes in process conditions, but also reveals that the crystallinity and morphology of the resulting NRs is sensitively dependent on process conditions (particularly the choice of substrate).

2. Experimental

WO_x NRs were deposited on W (Goodfellow, as rolled, 99.95% purity), Ta (Testbourne, rolled bright annealed, 99.99% purity) and Cu (Goodfellow, annealed, 99.9% purity) foil substrates using apparatus that has been described previously.[26] The deposition chamber was evacuated using a rotary-backed turbomolecular pump, yielding a typical base pressure of $\sim 1 \times 10^{-6}$ Torr. The output of an ArF excimer laser (Coherent, COMPex Pro 102, 193 nm, 10 Hz repetition rate) was focused onto a rotating WO_3 target (Testbourne, hot pressed polycrystalline sample, 99.95% purity) at a 45° incident angle, yielding an incident fluence $F = 6$–10 J cm^{-2}. The resulting plume of ablated material propagates roughly symmetrically about the target surface normal and impinges on the substrate, which is positioned at a distance $D = 70$ mm from the target. Substrates were ultrasonically cleaned in acetone, then washed with 99.98% ethanol, dried in air, and attached to a 250 W tungsten halogen quartz bulb (used as a heater, and capable of maintaining the substrate temperature, T_{sub}, within 10 °C of any selected value in the range $25 \leq T_{sub} \leq 700$ °C) for the duration of the deposition, t. The chamber is designed to allow backfilling with a steady (10 sccm) flow of oxygen, hence providing for a background pressure in the range $0 \leq pO_2 \leq 100$ mTorr during the PLD stage. 'Base' conditions were taken to correspond to $pO_2 = 10$ mTorr.

The as-grown WO_x samples were characterized by field emission scanning electron microscopy (FE-SEM, JEOL6300LV), transmission electron microscopy (TEM, JEOL 1200EX), high resolution transmission electron microscopy (HRTEM, JEOL 2010), selected area electron diffraction (SAED, Philips EM430 TEM), X-ray diffraction (XRD, Bruker AXS D8 Advance powder diffractometer with Cu Kα radiation), Raman spectroscopy (Renishaw InVia spectrometer, 632.8 nm excitation), X-ray photoemission spectroscopy (XPS, Kratos Axis Ultra DLD photoelectron spectrometer with a monochromatic Al Kα source (1486.6 eV)), and their field emission properties investigated.

3. Results and discussion

Observations and analyses of WO_x NR samples grown on W, Ta and Cu substrates are presented and discussed in sequence. Experimental parameters (F, T_{sub}, t and pO_2) were varied in each case, but with particular emphasis on identifying process conditions that led to the richest nanostructure rather than seeking to maintain constancy across the three families of depositions. The various substrates were cleaned, successively, in acetone then ethanol in an ultrasonic bath, then dried with compressed air, but otherwise used as supplied. Only reflections attributable to the bare metal were identifiable by XRD, but we recognize that each substrate must be covered with a thin surface oxide layer from the very start of the PLD process.

3.1. Growth on W substrates

Heating a W substrate[28] (or a W film on a Si substrate[29]) in an oxygen-containing atmosphere is a known route to forming WO_x NRs. Environmental TEM studies of WO_x NR growth from a W wire maintained at $T_{sub} = 800$ °C in a low pressure of O_2 have led to the suggestion that growth is initiated by thermally induced cracking of the natural WO_x surface layer, formation of tungsten protrusions by diffusion through these cracks, and subsequent oxidation.[28] The SEM images shown in Fig. 1 allow
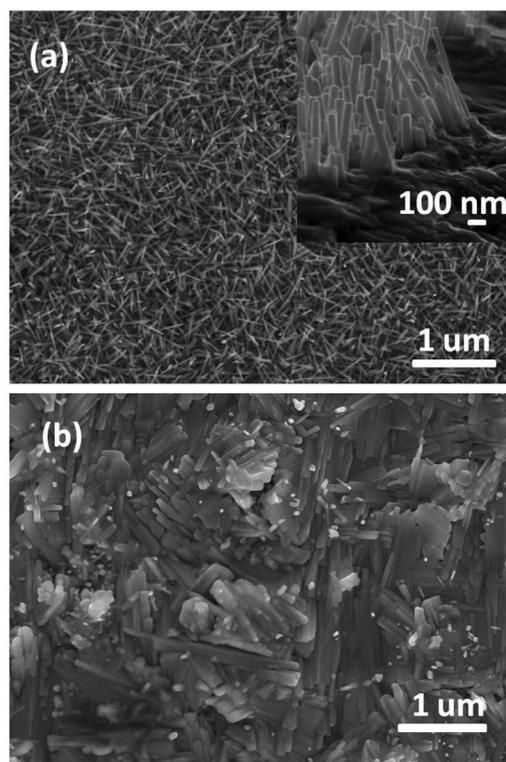
Fig. 1 SEM images of a WO_x layer grown on a W substrate at $T_{sub} = $ 700 °C in the presence of $pO_2 = 10$ mTorr for $t = 45$ min (a) with and (b) without the contribution from 193 nm ablation of the WO_3 target at $F = $ 10 J cm^{-2}. The inset in (a) shows a section (tilt view) through the PLD-assisted NR array obtained after cleaving the sample.

comparison of two WO_x NR samples grown on a W substrate under conditions that were identical (T_{sub} = 700 °C, pO_2 = 10 mTorr, t = 45 min) in all details bar one: sample (a) was grown with and sample (b) without the PLD contribution (*i.e.* the latter was produced by thermal oxidation only). The PLD-free sample (Fig. 1(b)) shows vestigial surface nodules and some coarse rod-like structures, but the with-PLD sample shows a dense covering of imperfectly aligned NRs, the details of which depend sensitively on the deposition conditions. As Fig. 2 shows, the NR coverage and the NR lengths in the with-PLD samples both increase greatly as T_{sub} is increased from 500 °C to 700 °C. Increasing pO_2 from 10 to 100 mTorr (at T_{sub} = 700 °C) results in shorter, thicker NRs.

Fig. 3(a) shows XRD spectra of the with-PLD WO_x-on-W sample shown in Fig. 1(a) and a sample from the polycrystalline target (scraped onto a Si support). The three peaks at $2\theta \sim$ 23–24.5° in the spectrum of the target material confirms its predominantly monoclinic nature (JCPDS no. 43-1035), whereas the XRD spectrum of the with-PLD (and the PLD-free) samples are dominated by the (200) and (400) reflections of cubic-WO_3 (JCPDS no. 46-1096, labelled according to a 7.6 Å unit cell) and the W substrate itself. The dominance of these reflections implies preferential (100) alignment, that we assume to be directed by the oxidizing substrate. Fig. 3(b) and (c) illustrate the effects of, respectively, increasing T_{sub} (at constant pO_2 = 10 mTorr) and increasing pO_2 (at constant T_{sub} =

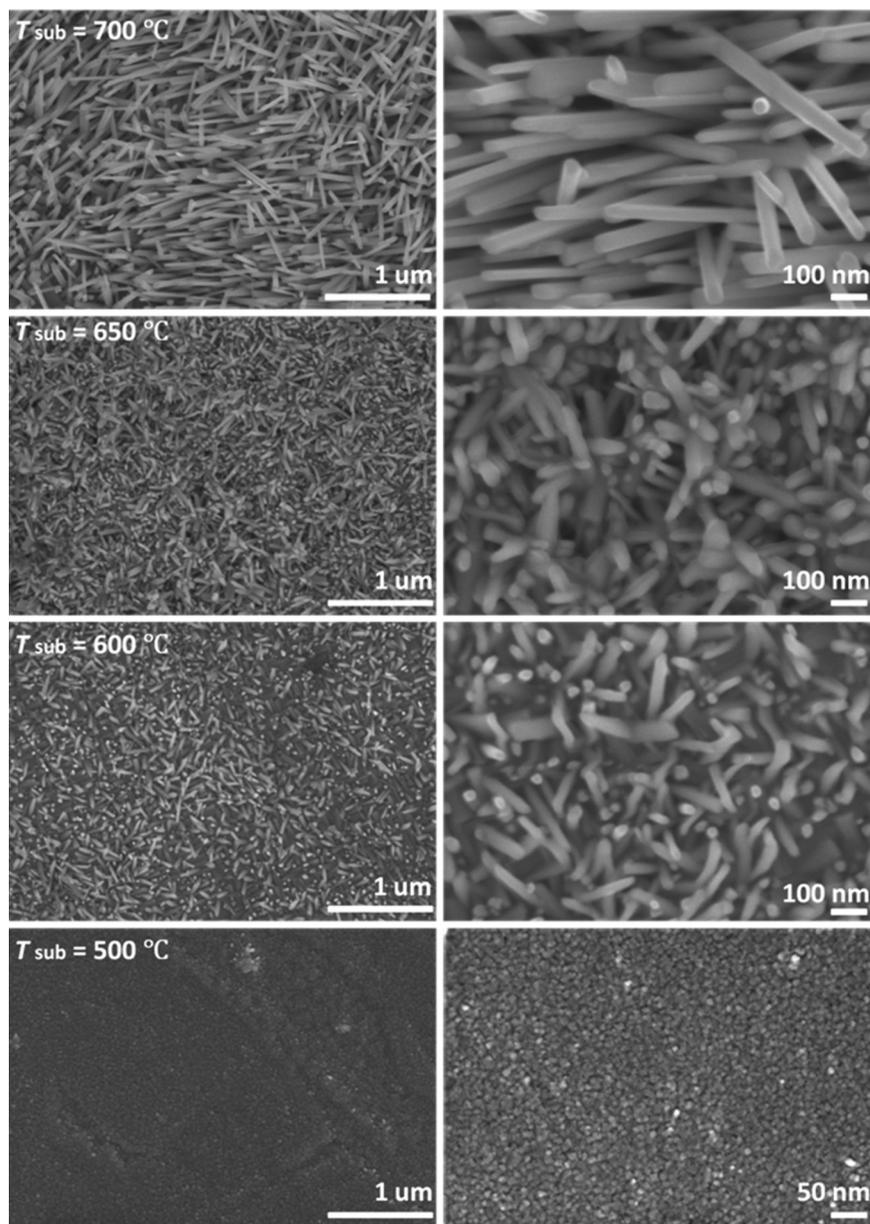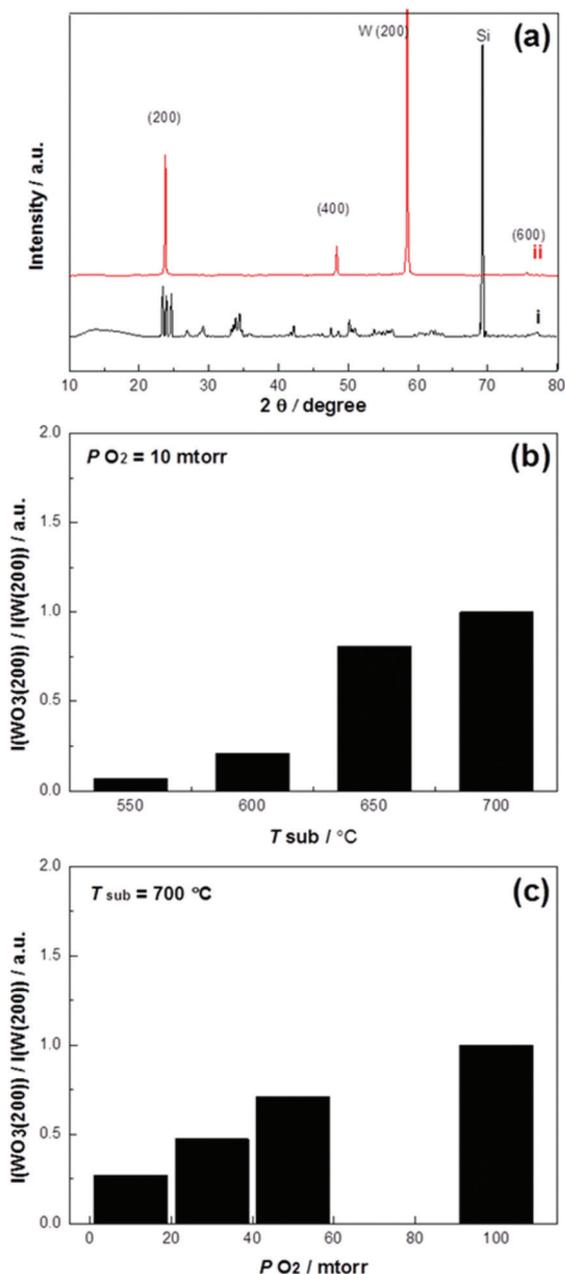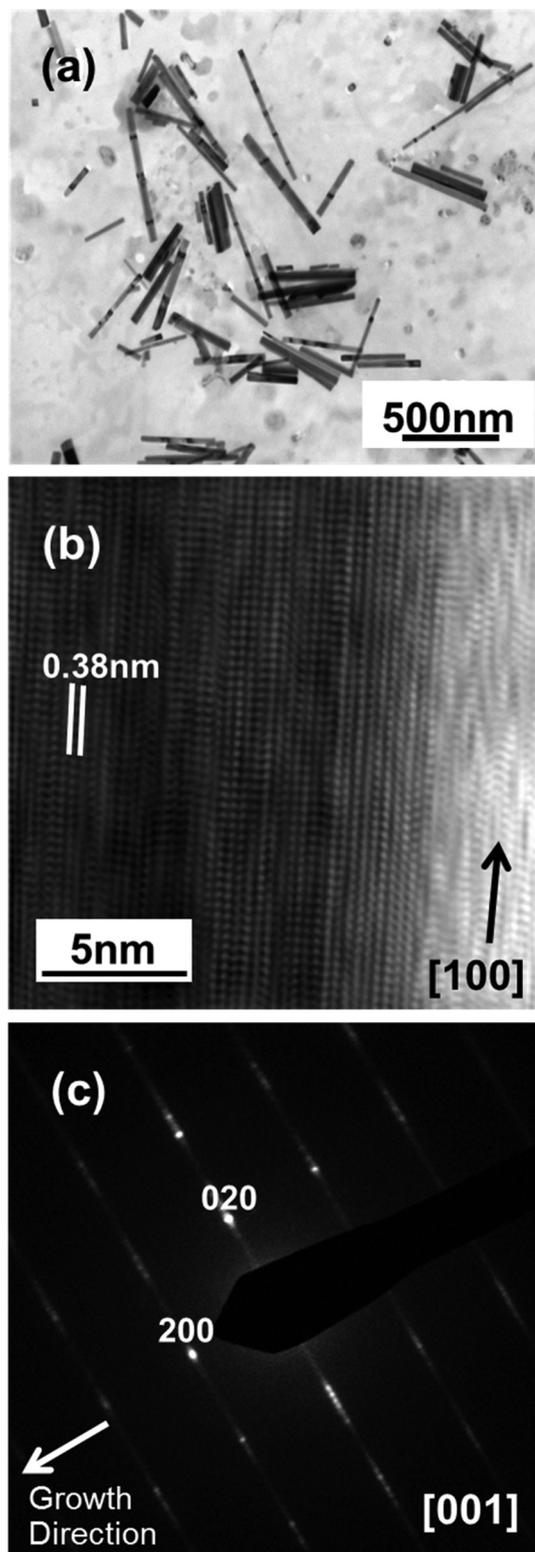

Fig. 2   Low and high resolution SEM images (left and right hand columns, respectively) illustrating the T_{sub} dependence of the morphology of the WO_x layer formed on a W substrate by 193 nm ablation of the WO_3 target at F = 10 J cm^{-2} in pO_2 = 10 mTorr for t = 45 min.

Fig. 3 (a) XRD spectra of (i) material scraped from the WO_3 target onto a Si substrate (that confirms the (predominantly) monoclinic structure of the target material) and (ii) the WO_x layer formed on a W substrate maintained at T_{sub} = 700 °C by 193 nm ablation of the WO_3 target at F = 10 J cm^{-2} in the presence of pO_2 = 10 mTorr for t = 45 min (the dominant peaks in which are attributable to (100) aligned cubic-WO_3 (as well as peaks from the underlying W substrate)). The lower panels show the way the relative intensities of the (200) reflections of WO_3 and W in XRD spectra of PLD-grown samples vary with (b) T_{sub} (at pO_2 = 10 mTorr) and (c) pO_2 (at T_{sub} = 700 °C). The ratios in (b) and (c) have been scaled such that the largest ratio in each case is 1.0.

Fig. 4 (a) Low resolution TEM image of material broken from the WO_x layer grown on a W substrate at T_{sub} = 700 °C in the presence of pO_2 = 10 mTorr for t = 45 min with the contribution from 193 nm ablation of the WO_3 target at F = 10 J cm^{-2}. (b) HRTEM image of the tip of a single NR, showing the d = 0.38 nm fringe spacing and an obvious stacking fault. (c) SAED pattern taken from this NR sample, indexed as cubic-WO_3.

700 °C) as evidenced by the relative intensities of the (200) reflections of WO_3 and W (at 2θ = 23.6 and 58.3°, respectively) – with the largest ratio in each plot arbitrarily scaled to 1.0. Clearly, increasing T_{sub} and pO_2 both have the effect of increas-

ing the relative intensity of the WO$_3$ reflection, but the relative intensities of the various WO$_3$ reflections in any one XRD spectrum show little sensitivity to these changes, and the main factor behind these trends is likely to be the amount of deposited material. By way of comparison, the corresponding ratio for the case of a PLD-free film grown for the same duration at T_{sub} = 700 °C and pO_2 = 10 mTorr is 0.22.

TEM analysis reveals further subtleties. The low resolution TEM image of material broken from the with-PLD sample (Fig. 4(a)) provides an estimate of the NR lengths (which reach $\ell \sim$ 700 nm) and diameters. The latter vary among the different NRs, spanning the range 50–80 nm, but remain fairly constant along the length of any one NR. Fig. 4(b) and (c) show, respectively, a HRTEM image from near the tip of a single NR and the SAED pattern recorded from this NR. The latter is consistent with a (001) orientation of cubic-WO$_3$ and a [100] growth direction – in accord with the XRD data (Fig. 3(c)) – while the obvious streaking in the (020) reflection implies the presence of numerous stacking faults in this direction. The closely spaced diffraction spots apparent in the diffraction streaks also suggest a long range ordering of the stacking faults. These observations are consistent with the HRTEM image (Fig. 4(b)), which shows single crystal regions with clearly defined fringe spacings of $d \sim$ 0.38 nm (characteristic of cubic-WO$_3$) separated by obvious stacking faults where the registry of the planes slips by, for example, half a fringe spacing. Such herring-bone-like patterns, which imply the presence of multiple superimposed crystallographic domains bounded by stacking faults, or crystallographic shears, have also been reported previously[16,30,31] and are a characteristic signature of sub-stoichiometric tungsten trioxide (WO$_{3-\delta}$).

3.2. Growth on Ta substrates

Similar process conditions enable growth of dense arrays of WO$_x$ NRs on Ta substrates. Optimal conditions were established as $T_{sub} \sim$ 700 °C and pO_2 = 50 mTorr, as illustrated by the SEM image of a with-PLD sample grown for t = 45 min shown in Fig. 5(c). As with a W substrate, the form of the deposited material is very sensitive to the choice of T_{sub}; deposition for the same t and with the same pO_2 but lower T_{sub} yielded either sparse clumps of NRs or none at all (Fig. 5(a) and (b)). Deposition at $T_{sub} \sim$ 700 °C but with lower pO_2 (e.g. 10 mTorr) again yielded dense NR arrays, but with smaller aspect ratio (as illustrated in Fig. 5(d)). XRD analysis reveals that the dominant phase evolves with T_{sub}. Fig. 6 shows XRD data from several samples grown at different T_{sub} but constant pO_2 = 50 mTorr; XRD spectra of samples grown in pO_2 = 10 mTorr show all the same trends. All peaks in the XRD spectra of samples prepared at $T_{sub} < $ 550 °C are attributable to the Ta foil substrate – consistent with the amorphous appearance of the WO$_x$ layer in the corresponding SEM image (Fig. 5(a)). Additional reflections are observed in the XRD spectra of samples deposited at $T_{sub} \geq$ 550 °C, all of which are seen (by SEM) to support NRs. None of the additional peaks can be assigned to cubic-WO$_3$ (Fig. 3), but most align well with documented low-order reflections from the hexagonal phase of WO$_3$ (JCPDS no. 33-1387).

Once again, however, TEM analysis reveals further subtleties. Low-resolution TEM images of NRs grown by PLD on Ta for t = 45 min at T_{sub} = 700 °C and pO_2 = 50 mTorr (Fig. 7(a)) show clear similarities with those of the NRs grown on W (Fig. 4(a)), but HRTEM and SAED investigations imply the

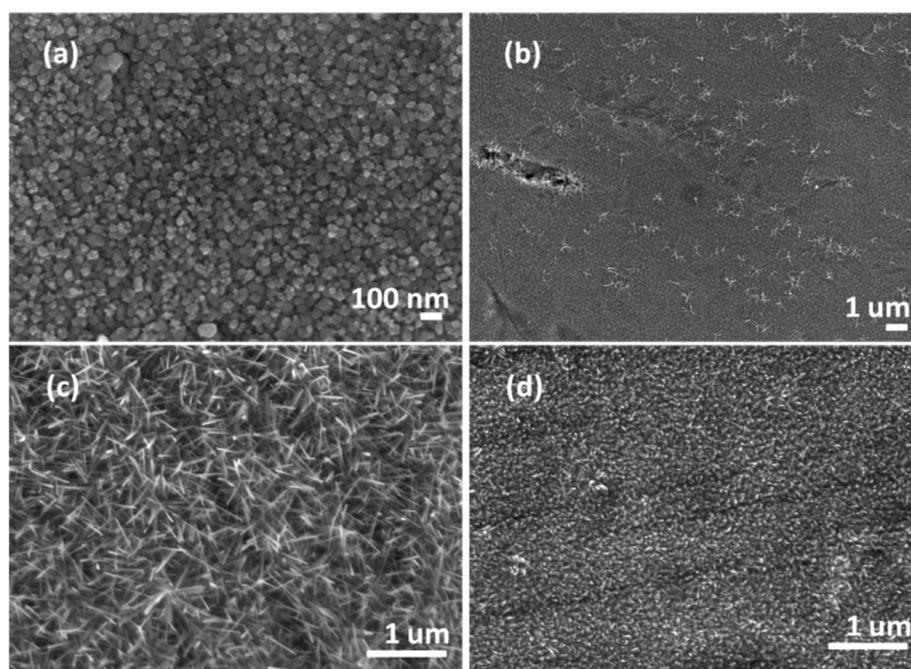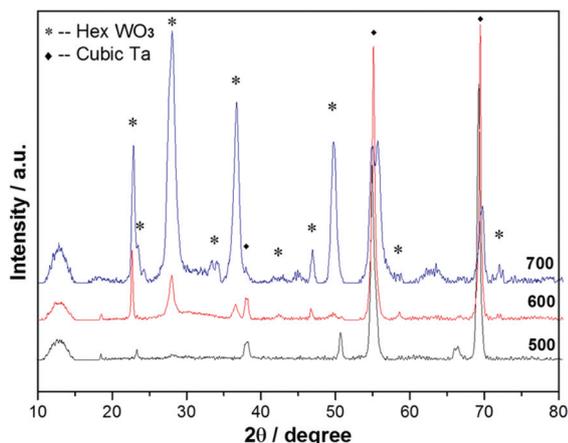Fig. 5 SEM images of WO$_x$ layers grown by 193 nm ablation of the WO$_3$ target for t = 45 min on Ta substrates under the following conditions of T_{sub} and pO_2: (a) 450 °C, 50 mTorr; (b) 550 °C, 50 mTorr; (c) 700 °C, 50 mTorr; (d) 700 °C, 10 mTorr.

**Fig. 6** XRD spectra of WO_x layers grown on Ta by 193 nm ablation of the WO_3 target for t = 45 min in pO_2 = 50 mTorr at T_{sub} = 500, 600 and 700 °C. Diffraction peaks attributable to hexagonal-WO_3 are evident in spectra of samples grown at T_{sub} ≥ 550 °C as indicated by the symbols above the upper most trace.

presence of more than one phase. The HRTEM images of all of the NRs subjected to detailed analysis show the $d \sim 0.38$ nm lattice spacing associated with cubic-WO_3 and very obvious stacking faults (see *e.g.* Fig. 7(b)); again, the associated SAED images show some streaking in the (020) reflection (Fig. 7(c)). Electron diffraction patterns taken from larger areas (*e.g.* from a clump of NRs, Fig. 7(d)) show a more complex pattern of diffraction rings, the separations between which imply a dominant contribution from hexagonal WO_3 [32] – as implied by the XRD data (which is also taken from areas much larger than that of a single NR). Thus we conclude that PLD on Ta substrates at T_{sub} ≥ 550 °C yields both cubic and hexagonal WO_{3-x}. XRD analysis suggests a predominance of hexagonal phase material in the total deposit, but the HRTEM studies indicated that many of the better formed NRs have a cubic crystal structure.

3.3. Growth on Cu substrates

Tungsten oxide NRs were also successfully grown on Cu substrates but, as Fig. 8 and 9 show, these have a very different morphology. Again, we identify an optimum process window as illustrated by the SEM images shown in Fig. 8, all of which
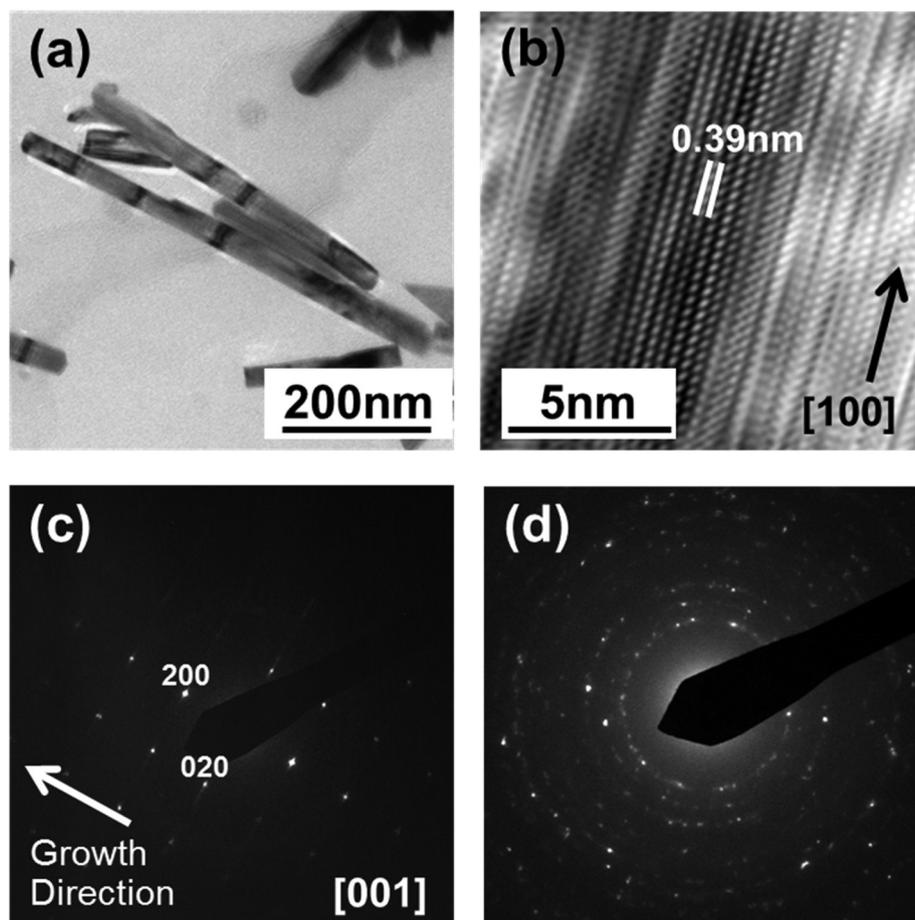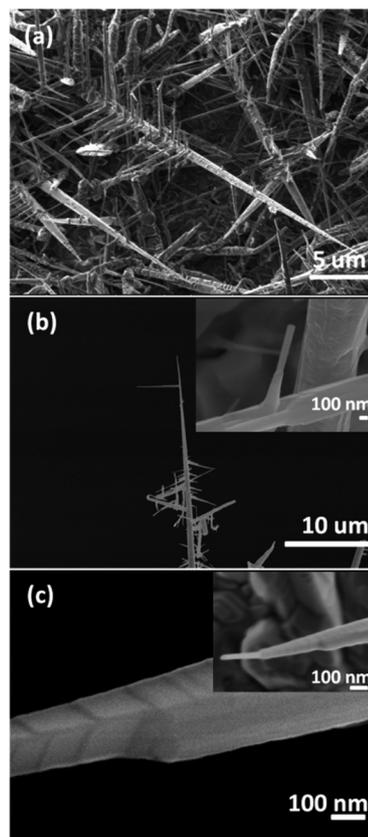

Fig. 7 (a) Low resolution TEM image of NRs broken from the WO_x layer grown on a Ta substrate at T_{sub} = 700 °C by 193 nm ablation of the WO_3 target in the presence of pO_2 = 50 mTorr for t = 45 min. (b) HRTEM and (c) SAED images taken from a single NR, illustrating the cubic-WO_3 microstructure. (d) SAED image taken from a clump of NRs; the ring separations fit well with that expected for hexagonal WO_3.
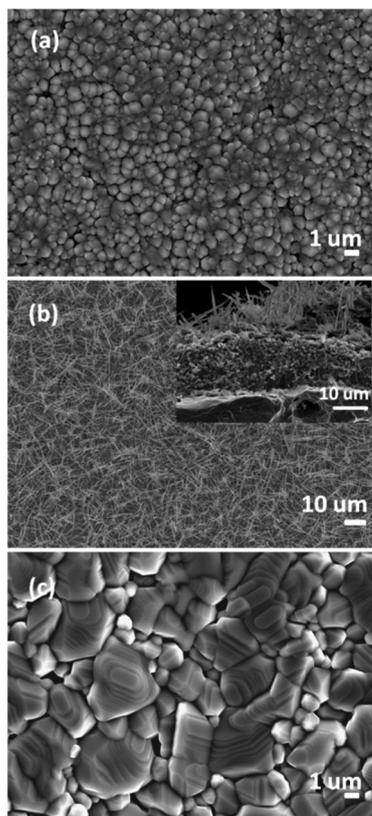
Fig. 8 SEM images of WO_x layers grown by 193 nm ablation of the WO_3 target for t = 45 min on a Cu substrate in the presence of pO_2 = 10 mTorr at T_{sub} = (a) 400 °C; (b) 500 °C; and (c) 600 °C. The cross-section image of the deposit grown at T_{sub} = 500 °C (inset in panel (b)) shows a tangle of poorly aligned NRs emerging from a dense thatch of underlying material.

Fig. 9 Progressively higher resolution SEM images of WO_x NRs grown on a Cu substrate in the presence of pO_2 = 10 mTorr by 193 nm ablation of the WO_3 target for t = 45 min at T_{sub} = 500 °C: (a) an as-grown tangle of tree-like NRs; (b) a 'single' NR demonstrating the emergence of first (and in some cases second) generation daughter NRs at right angles to and from the edge of (see inset) the shaft of the parent NR; (c) detail of the end of a single NR shaft, illustrating obvious faceting and tapered morphology in the growth direction.

samples were deposited under pO_2 = 10 mTorr for t = 45 min. The morphology of the deposited material is very sensitive to T_{sub}, and ranges from a 'cobbled' coating at T_{sub} = 400 °C, through an array of fine NRs at T_{sub} = 500 °C, to a film composed of larger crystallites at 600 °C. The cross-section image (Fig. 8(b), inset) shows that the NRs on Cu are less dense than those on Ta or W substrates, and sit on a dense underlying thatch of deposited material. The very different appearance of these NRs (cf. those grown on W or Ta substrates) is shown more clearly by the image of an as-grown tangle of NRs (Fig. 9(a)) and of a 'single' NR in Fig. 9(b). The NR has a 'tree-like' appearance, with first- (and in some cases second-) generation 'daughter' NRs emerging perpendicular to the shaft of the parent NR. These dendritic structures are somewhat reminiscent of those reported in prior studies where W foil (covered by a SiO_2 plate) was heated in Ar at 1600 °C,[33] where W powder was heated in oxygen to 1400–1450 °C,[6,34] and where PLD-grown WO_x films were subsequently thermally annealed in vacuum and then in air.[35] The daughter NRs in the present work appear to grow from an edge of the parent NR, as shown in the inset to Fig. 9(b), rather than the face (as suggested by some of these prior studies). Compared with the WO_x NRs grown on W and Ta, the NRs grown on Cu are

'macroscopic': many μm in length, generally much thicker at the base, and clearly tapering in the growth direction; many terminate with a narrow tip (Fig. 9(c)).

As Fig. 10 shows, the as-grown material exhibits a simple XRD spectrum with clear peaks at 2θ = 15.2, 18.1, 31.6 and 36.2° that are not attributable to the Cu substrate. We have not succeeded in matching these with any documented WO_x structure, though we note that peaks at ~18° and ~37° have previously been identified as (111) and (222) reflections of orthorhombic WO_3.[36] As noted above, the XRD measurements inherently sample a large (~1 cm²) area, so the relative contributions made by the dendritic NRs and the underlying thatch to the total XRD spectrum is unclear. The SAED patterns shown in Fig. 11, in contrast, are taken from the tapered tip of a single NR and are clearly consistent with a cubic structure with lattice parameter a = 0.38 nm. Panel (a) in Fig. 11 shows a (001) diffraction pattern (i.e. with an [001] zone axis parallel to the electron beam direction) with the NR growth direction [100] indicated by the arrow, while Fig. 11(b) shows the corresponding SAED pattern taken along the [101] axis (obtained by
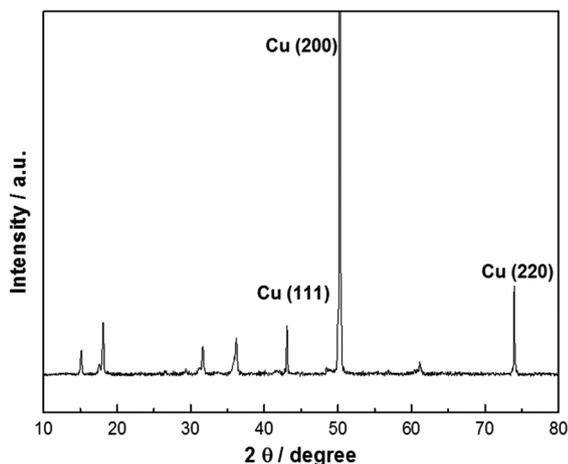
Fig. 10 XRD spectrum of the WO_x layer grown on Cu by 193 nm ablation of the WO_3 target for t = 45 min in pO_2 = 10 mTorr and at T_{sub} = 500 °C. Peaks attributable to the Cu substrate are assigned, leaving four unassigned peaks that we attribute to WO_x.

tilting the NR by 45° about [010], such that the (040) reflection is common to both patterns). The appearance of the (020) reflection in the [101] pattern but not in the [001] pattern is consistent with {200} reflections being kinematically forbidden, with excitation depending on double diffraction routes which are present in the [101], but not in the [001], orientation.

Fig. 12(a) and (b) show an HRTEM image and an SAED pattern taken from the ends of other tapered crystals like that shown in the inset to Fig. 8(c). The SAED pattern is clearly different from those in Fig. 11 but if, for simplicity, we take the NR axis to be a [100] axis of the tip crystal, we can identify the main reflections nominally as {400}-type, with spacings of 0.19 nm that match well with the spacing of the {400} reflections identified in Fig. 11. The pair of spots arrowed in Fig. 12(b) can be reproduced by a model of the type shown in Fig. 12(d), based on W_nO_{3n-1} structures, where crystallographic

shear faults separate n planes of corner sharing WO_6 octahedra.[30,31] The structure and simulated diffraction pattern shown in Fig. 12(d) and (c) correspond to n = 4, *i.e.* W_4O_{11}. Experimentally, there is prominent streaking perpendicular to the NR axis, rather than the regular superlattice in Fig. 12(c), suggesting that n and the corresponding stoichiometry vary on a fine scale. These features are consistent with the lattice image in Fig. 12(a) (taken from a different crystal), which shows small regions that display a regular and approximately square cross-grating pattern, with 0.38 nm spacing, as well as an irregular structure perpendicular to the NR axis.

Selected WO_x samples grown on Cu were also investigated by XPS though, as with XRD, we caution that XPS analysis must return a superposition of compositional information for both the NRs and the underlying thatch. Expanded views of the W 4f and O 1s binding energy regions are shown in Fig. 13. The former can be decomposed (Fig. 13(a)) into a doublet of doublets, attributable to the $4f_{7/2}$ and $4f_{5/2}$ peaks of both the W^{6+} and W^{5+} oxidation states.[37,38] The presence of two oxidation states provides further indication that the material is sub-stoichiometric $WO_{3-\delta}$, as does the obvious tailing of the O 1s peak to higher binding energies (Fig. 13(b)). The illustrative decomposition shown in Fig. 13(b), along with an assumed assignment of the 530.2 and 531.4 eV peaks to O atoms in, respectively, stoichiometric WO_3 and sub-stoichiometric $WO_{3-\delta}$,[39,40] implies a mean composition with $\delta \approx 0.2$.

3.4. Raman spectroscopy of as-grown WO_x samples

Features in Raman spectra of WO_x samples are traditionally viewed in three separate wavenumber regions, depending on their physical origin. Peaks at wavenumbers <200 cm^{-1} are associated with lattice modes (tilting or translations of the WO_6 octahedra); features in the 200–400 cm^{-1} region can be assigned to W–O–W stretch and/or O–W–O bending modes; while O–W–O stretching modes typically fall in the 600–900 cm^{-1} range.[41,42] The Raman spectrum of the polycrys-
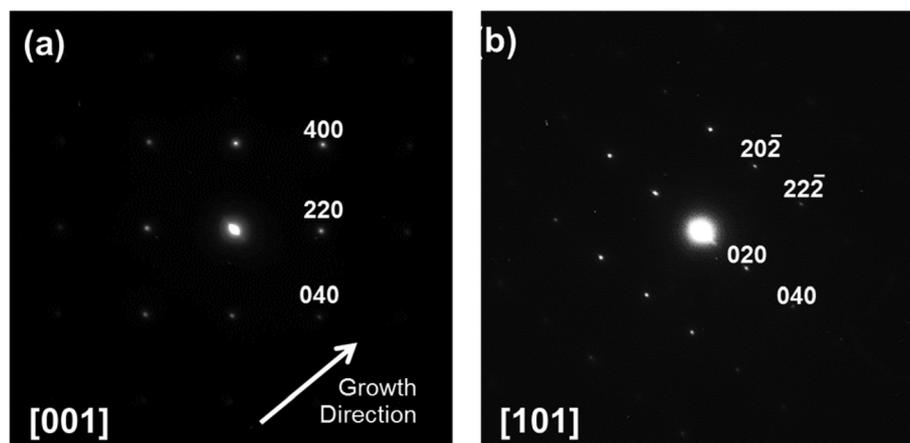

Fig. 11 SAED patterns recorded from near the tip of a single WO_x NR grown on Cu by 193 nm ablation of the WO_3 target for t = 45 min in pO_2 = 10 mTorr and at T_{sub} = 500 °C. Image (a) shows a (001) diffraction pattern (*i.e.* with an [001] zone axis parallel to the electron beam direction), with the arrow indicating the NR growth direction [100], while (b) shows the corresponding pattern taken along the [101] axis (obtained by tilting the NR by 45° about [010]). The (040) reflection is thus common to both patterns.
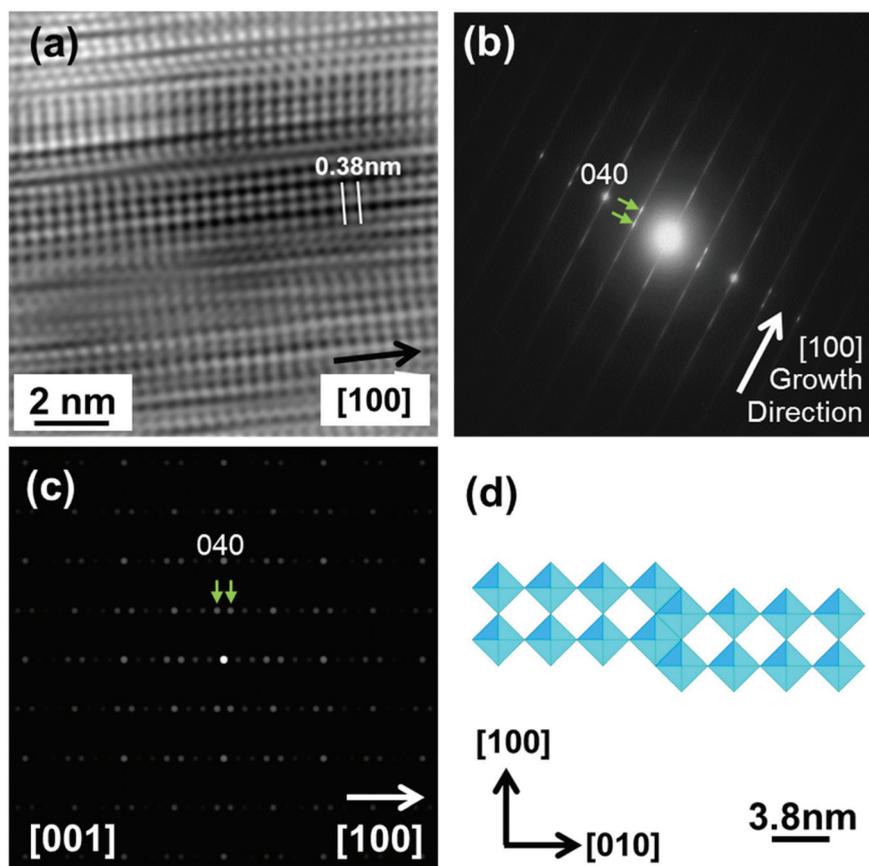
Fig. 12 (a) HRTEM and (b) SAED images recorded near the tip of single WO_x NRs grown on Cu by 193 nm ablation of the WO_3 target for t = 45 min in pO_2 = 10 mTorr and at T_{sub} = 500 °C, (c) simulated diffraction pattern for the model structure shown in (d), a unit cell for a W_4O_{11} structure where crystallographic shear faults separate 4 planes of corner sharing WO_6 octahedra. The two arrowed reflections in (c) can be compared with those arrowed in (b).
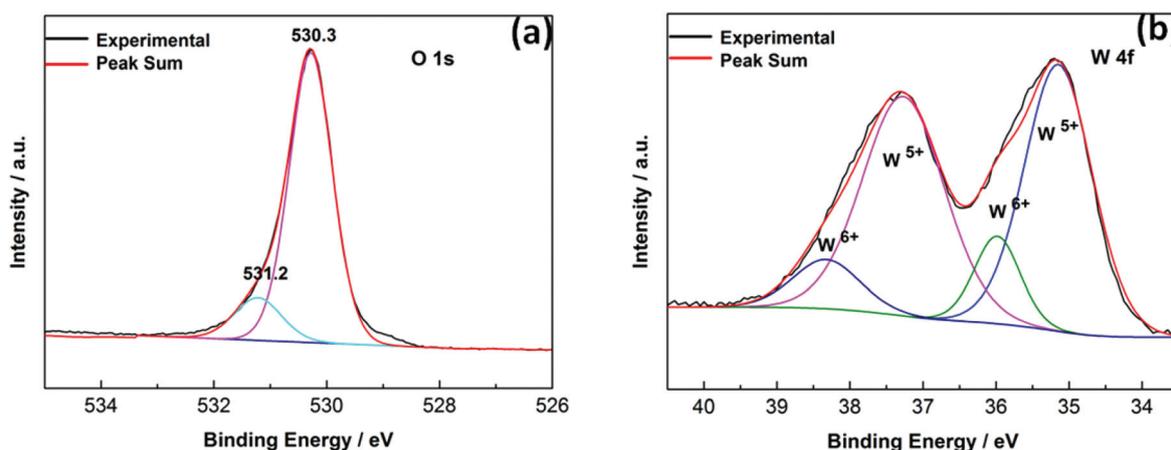

Fig. 13 Detailed views of the O 1s and W 4f peaks in the X-ray photoelectron spectrum of the WO_x-on-Cu sample grown by 193 nm ablation of the WO_3 target for t = 45 min in pO_2 = 10 mTorr and at T_{sub} = 500 °C, decomposed as described in the text.

talline target recorded under 632.8 nm illumination (curve (a) in Fig. 14) shows clear features at 273, 324, 716 and 807 cm^{-1}, all of which are characteristic of monoclinic WO_3. However, the additional weak features at 182 and 569 cm^{-1} (which match no documented Raman peaks of monoclinic WO_3) hint

at some contribution from other phases. Both of these conclusions accord well with the preceding XRD analysis.

Curves (b), (c) and (d) in Fig. 14 show Raman spectra of NR-rich deposits grown on W, Ta and Cu substrates, respectively. (b) and (c) both show broad features centered around 273, 716
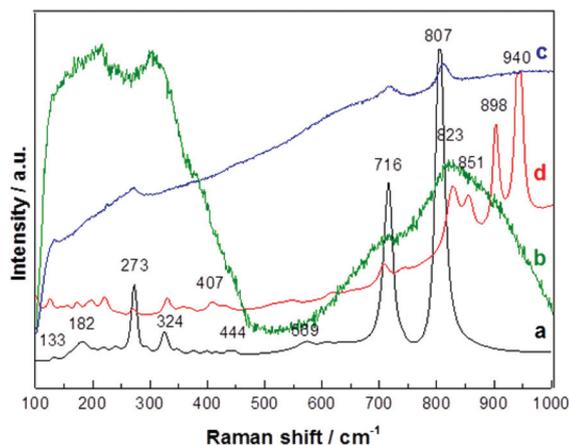
Fig. 14 Raman spectra (632.8 nm excitation) of (a) the polycrystalline WO_3 target and of the NR-rich WO_x deposits grown on (b) W, (c) Ta and (d) Cu substrates by 193 nm ablation of the WO_3 target for t = 45 min using pO_2 and T_{sub} values appropriate for optimal NR growth in each case. Wavenumbers of many of the more prominent peaks are super-imposed above the relevant trace.

and 807 cm^{-1}, but the breadth of these features (which must involve scattering from both the NRs and the underlying thatch) limits the utility of Raman spectroscopy as a compositional diagnostic in these cases. Curve (d) shows much more structure, with the peaks at high wavenumber particularly notable. Based on the previous literature,[41] it is tempting to assign the 823 and 851 cm^{-1} features to O–W–O stretching modes, with the shift to higher wavenumber reflecting some shortening (stiffening) of the relevant bonds between the edge sharing octahedra. The 940 cm^{-1} feature is associated with terminal W=O bonds. This feature is commonly observed in the Raman spectra of nanocrystalline WO_x samples; indeed, arguments have appeared[43] suggesting that its intensity relative to that of the O–W–O stretch bands can be used as a measure of surface-to-volume ratio or cluster size. The present data may lend some support to this argument given that these features are particularly evident in the Raman spectrum of material deposited on a Cu substrate which, as Fig. 9 showed, is rich in the dendritic NR structures.

3.5. Field emission measurements on as-grown WO_x samples

Field emission (FE) measurements were performed at room temperature in a test chamber (base pressure ~5 × 10^{-7} Torr) that has been described previously.[44] The WO_x samples acted as the cathode, the anode comprised a phosphor screen coated with a 10 nm layer of gold, and the cathode–anode separation was maintained at d = 420 μm using a silica spacer and an aperture that defines an effective sampling area A = 0.076 cm^2. The voltage, V, applied to each sample was ramped up and down once and the emission current, I, measured to obtain an initial I–V curve, and the sample was then 'conditioned' by cycling a further 5 times to encourage the release of any impurities.
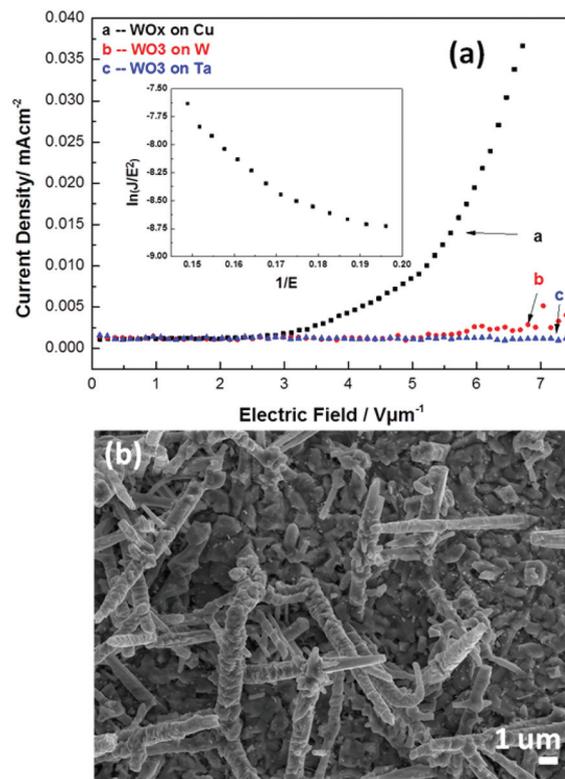
Fig. 15 (a) Field emission current *vs.* applied field plot for a NR-rich WO_x deposit on a Cu substrate grown under conditions as for the material shown in Fig. 9(a), along with the corresponding Fowler–Nordheim plot (inset). (b) SEM image of such a sample after application of a 12 V μm^{-1} field, illustrating the destruction of the finer nanostructures caused by over-driving the emission.

The I–V data shown in Fig. 15(a) for NR-rich WO_x samples grown on W, Ta and Cu substrates are the average values returned from the next 10 up-down cycles. As is customary, we plot the emission current density, J (= I/A, in mA cm^{-2}) *vs.* electric field, E (= V/d, in V μm^{-1}). Only the sample grown on Cu exhibits encouraging FE properties, with a turn on field (which we choose to define as the field yielding an emission current density of 10 μA cm^{-2}) of ~5 V μm^{-1} –comparable to that reported for nanostructured WO_x samples in other recent studies.[45–47] The associated Fowler–Nordheim plot[48] (*i.e.* plot of ln(J/E^2) *vs.* 1/E, which is shown as an inset to Fig. 15(a)), shows two linear regions (with a steeper slope in the high field region) pivoting at 1/E ~ 0.17 V^{-1} μm. The form of this plot is reminiscent of that reported in a previous study of FE from WO_x nanowires grown on electrochemically sharpened tungsten tips[49] and, as in that case, can plausibly be attributed to the disperse spread of NR lengths, diameters and orientations supported by the sample.

The stability of the FE from a NR-rich WO_x on Cu sample was examined at a fixed (6.1 V μm^{-1}) field by logging the current every 1.3 s. Apart from some transient spikes, the emission remained stable at ~15 μA (fluctuating by <10%) over the duration of the measurement (35 hours). SEM analysis of this sample post FE testing showed no discernible change to the

sample morphology, but ramping the field up to 12 V μm^{-1} resulted in an immediate and dramatic drop in emission intensity. The SEM image of this over-driven sample (Fig. 15(b)) reveals large structural changes; the finer tips and branches have been destroyed, leaving just the parent NR shafts with a much rougher surface morphology.

4. Conclusions

The present study reports the growth of tungsten oxide NRs by 193 nm pulsed laser deposition in a low background pressure of oxygen, and subsequent characterisation of the as-grown material by SEM and HRTEM, SAED, XRD, Raman and XPS. The morphology of the deposited material is found to be sensitively dependent upon the choice of deposition conditions, including the substrate material itself. HRTEM analysis shows that NRs formed on W, Ta and Cu substrates each grow along the [100] direction and display obvious stacking faults running along this direction. Such faults also reveal themselves by streaking in the SAED pattern, perpendicular to the growth axis – implying that the NR composition is sub-stoichiometric $WO_{3-\delta}$ in each case. The NR morphologies are very different, however. NRs formed on W or Ta substrates are short (100 s of nm in length) and display uniform cross-sections, while those grown on the Cu substrate are typically longer, thicker, tapered, and display a branched, dendritic microstructure. Only these latter NRs are found to give significant field emission.

References

1 H. D. Zheng, J. Z. Ou, M. S. Strano, R. B. Kaner, A. Mitchell and K. Kalantar-Zadeh, *Adv. Funct. Mater.*, 2011, **21**, 2175, and references therein.

2 C. G. Granqvist, *Handbook of Inorganic Electrochromic Materials*, Elsevier, New York, 1995.

3 G. A. Niklasson and C. G. Granqvist, *J. Mater. Chem.*, 2007, **17**, 127.

4 See, for example, Z. G. Zhao and M. Miyauchi, *Angew. Chem., Int. Ed.*, 2008, **47**, 7051.

5 See, for example, X. Liu, F. Wang and Q. Wang, *Phys. Chem. Chem. Phys.*, 2012, **14**, 7894.

6 A. Ponzoni, E. Comini, G. Sberveglieri, J. Zhou, S. Z. Deng, N. S. Xu, Y. Ding and Z. L. Wang, *Appl. Phys. Lett.*, 2006, **88**, 203101.

7 R. S. Devan, R. A. Patil, J. H. Lin and Y. R. Ma, *Adv. Funct. Mater.*, 2012, **22**, 3326, and references therein.

8 See, for example, H. Zheng, Y. Tachibana and K. Kalantar-Zadeh, *Langmuir*, 2010, **26**, 19148.

9 J. G. Allpress, R. J. D. Tilley and M. J. Sienko, *J. Solid State Chem.*, 1971, **3**, 440.

10 Z. J. Gu, T. Y. Zhai, B. F. Gao, X. H. Zheng, Y. B. Wang, H. B. Fu, Y. Ma and J. N. Yao, *J. Phys. Chem. B*, 2006, **110**, 23829.

11 J. M. Wang, E. Khoo, P. S. Lee and J. Ma, *J. Phys. Chem. C*, 2008, **112**, 14306.

12 K. Kalantar-Zadeh, A. Vijayaraghavan, M.-H. Ham, H. D. Zheng, M. Breedon and M. S. Strano, *Chem. Mater.*, 2010, **22**, 5660.

13 H. W. Zhang, G. T. Duan, Y. Li, X. X. Xu, Z. F. Dai and W. P. Cai, *Cryst. Growth Des.*, 2012, **12**, 2646.

14 H. W. Zhang, Y. Li, G. T. Duan, G. Q. Liu and W. P. Cai, *CrystEngComm*, 2014, **16**, 2491.

15 J. Thangala, S. Vaddiraju, R. Bogale, R. Thurman, T. Powers, B. Deb and M. K. Sunkara, *Small*, 2007, **3**, 890.

16 A. M. Smith, M. G. Kast, B. A. Nail, S. Aloni and S. W. Boettcher, *J. Mater. Chem. A*, 2014, **2**, 6121.

17 F. Mitsugi, E. Hiraiwa, T. Ikegami, K. Ebihara and R. K. Thareja, *Jpn. J. Appl. Phys., Part 1*, 2002, **41**, 5372.

18 T. Aoki, T. Matsushita, A. Suzuki, K. Tanabe and M. Okuda, *J. Vac. Sci. Technol., A*, 2005, **23**, 1325.

19 C. V. Ramana, S. Utsunomiya, R. C. Ewing, C. M. Julien and U. Becker, *J. Phys. Chem. B*, 2006, **110**, 10430.

20 Y. Suda, H. Kawasaki, T. Ohshima and Y. Yagyuu, *Thin Solid Films*, 2008, **516**, 4397.

21 K. J. Lethy, D. Beena, R. V. Kumar, V. P. M. Pillai, V. Ganesan and V. Sathe, *Appl. Surf. Sci.*, 2008, **254**, 2369.

22 N. Santo, M. Filipescu, P. M. Ossi and M. Dinescu, *Appl. Phys. A*, 2010, **101**, 325.

23 Y. S. Zou, Y. C. Zhang, D. Lou, H. P. Wang, L. Gu, Y. H. Dong, K. Dou, X. F. Song and H. B. Zeng, *J. Alloys Compd.*, 2014, **583**, 465.

24 M. H. Yaacob, J. Z. Ou, W. Wlodarski, C. S. Kim, J. Y. Lee, Y. H. Kim, C. M. Oh, K. P. Dhakal, J. Y. Kim and J. H. Kang, *J. Korean Phys. Soc.*, 2012, **60**, 393.

25 M. Z. Ahmad, J. Kang, A. S. Zoolfakar, A. Z. Sadek and W. Wlodarski, *J. Nanosci. Nanotechnol.*, 2013, **13**, 8315.

26 Y. Sun, G. M. Fuge and M. N. R. Ashfold, *Chem. Phys. Lett.*, 2004, **396**, 21.

27 G. M. Fuge, T. M. S. Holmes and M. N. R. Ashfold, *Chem. Phys. Lett.*, 2009, **479**, 125.

28 T. Tokunaga, T. Kawamoto, K. Tanaka, N. Nakamura, Y. Hayashi, K. Sasaki, K. Kuroda and T. Yamamoto, *Nanoscale Res. Lett.*, 2012, **7**, 85.

29 S. G. Jeon and J. J. Yong, *J. Mater. Res.*, 2008, **23**, 132.

30 T. Miyano, M. Iwanishi, C. Kaito and M. Shiojiri, *Jpn. J. Appl. Phys.*, 1983, **22**, 863.

31 J. Sloan, J. L. Hutchinson, R. Tenne, Y. Feldman, T. Tsirlina and M. Honyonfer, *J. Solid State Chem.*, 1990, **144**, 100.

32 B. Gerand, G. Nowogrocki, J. Guenot and M. Figlarz, *J. Solid State Chem.*, 1979, **29**, 429.

33 Y. Q. Zhu, W. B. Hu, W. K. Hsu, M. Terrones, N. Grobert, J. P. Hare, H. W. Kroto, D. R. M. Walton and H. Terrones, *Chem. Phys. Lett.*, 1999, **309**, 327.

34 J. Zhou, Y. Ding, S. Z. Deng, L. Gong, N. S. Xu and Z. L. Wang, *Adv. Mater.*, 2005, **17**, 2107.

35 A. Ponzoni, V. Russo, A. Bailini, C. S. Casari, M. Ferroni, A. Li Bassi, A. Migliori, V. Morandi, L. Ortolani, G. Sberveglieri and C. E. Bottani, *Sens. Actuators, B*, 2011, **153**, 340.

36 S. Rajagopal, D. Nataraj, D. Mangalaraj, Y. Djaoued, J. Robichaud and O. Y. Khyzhun, *Nanoscale Res. Lett.*, 2009, **4**, 1335.

37 H. Y. Wong, C. W. Ong, R. W. M. Kwok, K. W. Wong, S. P. Wong and W. Y. Cheung, *Thin Solid Films*, 2000, **376**, 131.

38 H.-S. Shim, J. W. Kim, Y.-E. Sung and W. B. Kim, *Sol. Energy Mater. Sol. Cells*, 2009, **93**, 2062.

39 S. Pal and C. Jacob, *Appl. Surf. Sci.*, 2007, **253**, 3317.

40 F. Y. Xie, L. Gong, X. Liu, Y. T. Tao, W. H. Zhang, S. H. Chen, H. Meng and J. Chen, *J. Electron Spectrosc. Relat. Phenom.*, 2012, **185**, 112.

41 M. F. Daniel, B. Desbat, J. C. Lassegues, B. Gerand and M. Figlarz, *J. Solid State Chem.*, 1987, **67**, 235.

42 C. Santato, M. Odziemkowski, M. Ulmann and J. Augustynski, *J. Am. Chem. Soc.*, 2001, **123**, 10639.

43 T. Kubo and Y. Nishikitani, *J. Electrochem. Soc.*, 1998, **145**, 1729.

44 Y. Zou, P. W. May, S. M. C. Vieira and N. A. Fox, *J. Appl. Phys.*, 2012, **112**, 044903.

45 Y. B. Li, Y. Bando and D. Golberg, *Adv. Mater.*, 2003, **15**, 1294.

46 J. G. Liu, Z. J. Zhang, Y. Zhao, X. Su, S. Liu and E. G. Wang, *Small*, 2005, **1**, 310.

47 F. Liu, T. Y. Guo, Z. Xu, H. B. Gan, L. F. Li, J. Chen, S. Z. Deng, N. S. Xu, D. Golberg and Y. Bando, *J. Mater. Chem. C*, 2013, **1**, 3217, and references therein.

48 R. H. Fowler and L. W. Nordheim, *Proc. R. Soc. London, Ser. A*, 1928, **119**, 173.

49 R. Seelaboyina, J. Huang, J. Park, D. H. Kang and W. B. Choi, *Nanotechnology*, 2005, **17**, 4840.